Aerospace Science and Technology 113 (2021) 106673

Contents lists available at ScienceDirect

Aerospace Science and Technology

www.elsevier.com/locate/aescte

Analysis, planning and control for cooperative transportation of tethered multi-rotor UAVs

Ya Liu [a,b], Fan Zhang [a,b,*], Panfeng Huang [a,b], Xiaozhen Zhang [a,b]

[a] The Research Center for Intelligent Robotics, School of Astronautics, Northwestern Polytechnical University, Xi'an, Shaanxi 710072, China
[b] The National Key Laboratory of Aerospace Flight Dynamics, Xi'an, Shaanxi 710072, China

ARTICLE INFO

Article history:
Received 6 November 2020
Received in revised form 28 February 2021
Accepted 19 March 2021
Available online 29 March 2021
Communicated by Xiande Fang

Keywords:
Tethered multi-rotor UAVs
Cooperative manipulation
Available wrench set
Tension distribution
Fixed-time ESO based control

ABSTRACT

The calculation of available wrench set of tethered multi-rotor UAVs is more challenging than that of the traditional cable-driven parallel robots (CDPRs) with fixed anchor points, due to the bounded thrust, motion acceleration and external disturbance acting on multi-rotor unmanned aerial vehicles (UAVs). To our best knowledge, this is the first work to investigate the dynamic available wrench set. We define an index called capacity margin to evaluate the robustness of the quasi-static motion for different system configurations and to represent the available maximum acceleration of the payload. Moreover, the feasible trajectories of multi-rotor UAVs are optimized using a tension distribution algorithm to accomplish the manipulation of the payload. Without the need of centralized ground control station, payload states and UAVs' velocity information, a decentralized output feedback control based on fixed-time extended state observer (ESO) is developed for the group of multi-rotor UAVs. The rigorous proof of stability of the closed-loop system is conducted. Finally, numerical simulations and comparative experiments are demonstrated to validate the proposed tension distribution algorithm and control strategy.

1. Introduction

1.1. Motivation

Compared to a single agent, multi-agent systems have become a high-profile subject of research for its improved capability, such as the UAVs formation, artificial satellites, distributed sensor networks, as well as autonomous underwater vehicles [1–3]. The multi-rotor UAVs with abilities of efficiency, agility, vertical takeoff and landing have received considerable attention for various applications such as remote sensing and photograph, entertainment, mine detection and civilian logistics. In view of the limited load capacity of single UAV or additional redundancy for safety, cooperative aerial manipulation by multiple multi-rotor UAVs has aroused research interest in manipulating a heavier or bulkier object that cannot be handled by an individual UAV [4]. In order to increase the load capacity, it is uneconomic to increase the size of the UAV. Moreover, when transporting a fragile or dangerous load, cooperative transportation can suppress the oscillations as the orientation of a large payload is easy to control by cooperative transportation [5]. Two basic approaches, namely grasped and tether-suspended payload manipulation have been introduced in [6].

Compared with the grasped payload manipulation method [7], tether suspended method will preserve the agility of the UAVs. The swinging of suspended payload during maneuvering with single multi-rotor UAV [8–10] can be suppressed by cooperative transportation. However, the tether-suspended system is underactuated, nonlinearly coupled and hybrid, due to no active control of payload and the multiple dynamical models of tethers [11]. We address these challenges by proposing a fixed-time ESO based output feedback control. To achieve this goal, we first analyze the dynamic available wrench set and maximum maneuver acceleration, then we optimize the trajectories of UAVs to respect the constraints and keep the tethers taut.

1.2. Related work

With the distinct feature, the tethered multi-rotor UAVs system has successfully attracted the attention of many researchers. Most recent research is focused on trajectory tracking controller design for the tether-suspended payload. In [12–14], the complete dynamic model of the cooperative transportation system with an arbitrary number of quadrotors was constructed based on the Lagrangian method. The corresponding geometric nonlinear controllers were designed such that the payload asymptotically follows

* Corresponding author at: 127 West Youyi Road, Beilin District, Xi'an Shaanxi, 710072, PR China.
E-mail address: fzhang@nwpu.edu.cn (F. Zhang).

https://doi.org/10.1016/j.ast.2021.106673
1270-9638/

a desired trajectory. Although the explicitly coupled feature of the transportation system was considered, some centralized controllers were designed. These controllers require the state feedback of the payload. In practice, it is difficult to obtain such feedback signal outdoors as the payload is a generic object without an inertial measurement unit (IMU). In [15], a set of flat outputs for the tethered multi-rotor UAVs system was chosen after proving the differential flatness of the system. However, the planning and control of the system are complicated with the requirement of higher-order derivatives. Simultaneously, the differential flatness property is sensitive to the external disturbance, uncertain parameters and unknown dynamics.

In [16], the direct relation between the motion of the quadrotors and the motion of the payload was derived. In [17], the coupled equations of motion for the multiple quadrotors carrying a rigid-body slung payload were obtained by the Kane's method. A path following controller was designed where only the quadrotors' state feedback is needed. However, the system can only implement an ordinary transportation task along a straight line at a given altitude and speed. In [18], the planning and control aspects for aerial robots with tether-suspended payload were investigated, while the authors assumed that the system is quasi-static and neglected the transients associated with the payload when deriving the controllers and planners. An indoor experiment was conducted in [18] using a Vicon motion capture system for positioning. Similarly, the cooperative control problem was investigated in [19]-[20] where a quasi-static payload was considered while neglecting the payload dynamics. In [21], the proportional-integral-derivative feedback control was implemented for cooperative transport of a slung load. Both the indoor and outdoor flight tests were implemented. However, the feasibility of the desired payload trajectory was not analyzed and the robustness of the designed controller cannot be guaranteed. Moreover, a new cooperative transportation system was proposed in our previous work [22], where the system is composed of multiple UAVs and a flexible net. The experiment verification is absent yet.

1.3. Contribution

The main contributions are threefold.

(1) The capacity margin is introduced to evaluate the available maximum acceleration of the payload. Compared with [23], where only the quasi-static system was considered, the available wrench analysis and capacity margin discussion for the tethered multi-rotor UAVs system with motion acceleration and external disturbance are implemented in this paper. Different from the traditional cable-driven parallel robots [24]-[25], the cooperative transportation system has moving pulley anchor points. To our best knowledge, it is the first work to investigate the dynamic available wrench set, which is more practical and challenging. Furthermore, an optimization-based trajectory generation method is proposed with accounting for the payload dynamics, collision avoidance and tension constraints.
(2) Compared with [12–15], where the centralized control methods are adopted, a decentralized control method is proposed where only the outputs of UAVs are needed. It is more convenient to realize in the outdoor environment without the ground control station and payload states information. In contrast to [17–20] where a quasi-static payload was considered neglecting the payload dynamics, a dynamic tracking task is discussed in this paper.
(3) This strategy is experimentally verified in both the indoor and outdoor environments. Some comparative experiments are conducted to validate the effectiveness of the algorithm.

The rest of this paper is stated as follows. Section 2 analyzes dynamic available wrench set in task space and capacity margin corresponding to a given configuration. In Section 3, the feasible trajectories for UAVs are generated by optimization-based method. Then, the system dynamics modeling and tracking controller design are implemented in Section 4. Moreover, numerical simulation, indoor and outdoor experiments are conducted in Section 5 and 6 respectively. Finally, Section 7 depicts the concluding remarks.

2. Available wrench and configuration analysis

It is extremely similar between tethered multi-rotor UAVs and CDPRs; indeed, the tethered multi-rotor UAVs system can be considered as a special CDPRs with moving pulley anchor points. For configuration design, workspace analysis, and trajectory generation, wrench capability analysis is an important research point for CDPRs [24]-[25]. Due to the actuation limits and dynamics of UAVs, the modeling of available wrench set of tethered multi-rotor UAVs system is different from the CDPRs. Simultaneously, it is more challenging than that of traditional CDPRs. In this section, the available wrench set of a tethered multi-rotor UAVs system has been analysis with different payload mass and formation configuration of UAVs. With the available wrench, the maximum acceleration of the payload can be determined with accounting for the constraints of UAVs actuation and dynamics. The available wrench set and capacity margin are discussed to evaluate the load capacity and robustness of the corresponding tethered multi-rotor UAVs transportation system in this paper. The available wrench set is also used for trajectory generation in the third part. Further, we will perform trajectory and configuration optimization for transportation system based on the available wrench set and capacity margin in the future.

2.1. Equilibrium conditions

This paper considers the cooperative transportation system with a point mass payload and N equal UAVs. The wrenches on the payload are generated through N tension vectors, gravity and external disturbance. As a result, the dynamics of the payload is formulated as follows:

$$m_p\ddot{r}_p = m_p g + \sum_{i=1}^{N} T_i q_i + d_p \tag{1}$$

where m_p is the mass of the payload, r_p is the position of the payload expressed in frame $\mathscr{F}_0$, g is the gravitational vector $[0\ 0\ -9.81]^T \mathrm{m\,s^{-2}}$, T_i is the tension in the i^{th} tether which connects the i^{th} UAV and payload, q_i is the unit vector from the payload to the attachment point on the i^{th} UAV, d_p is the external disturbance acting on the payload. For the translation motion of the i^{th} UAV, the actuation wrench is expressed in $\mathscr{F}_i$ as $f_i e_3$. The translation dynamics of the i^{th} UAV is expressed as follows:

$$m_i\ddot{r}_i = f_i R_i e_3 + m_i g - T_i q_i + d_i \tag{2}$$

where m_i is the mass of the i^{th} UAV, r_i is the position of the i^{th} UAV expressed in frame $\mathscr{F}_0$, f_i is the magnitude of the total thrust of the i^{th} UAV along $R_i e_3$, R_i is the rotation matrix from $\mathscr{F}_i$ to $\mathscr{F}_0$, d_i is the external disturbance working on the i^{th} UAV (see Fig. 1).

2.2. Available wrench set

Two mappings are proposed to express the available wrench set of a tethered multi-rotor UAVs system. One is the mapping from the thrust spaces of UAVs to the tension spaces, the other is from the tension spaces of the tether system to the wrench space of the

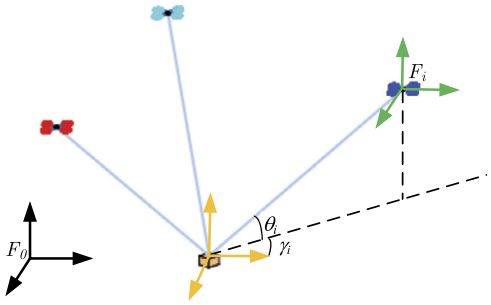

Fig. 1. Coordinate frames.

payload. Because a component of the actuation of the UAV is required to keep itself in the air, different configurations will result in variable tension spaces achievable by the tethered multi-rotor UAVs system, in turn affecting the set of available wrenches in task space. In the following, the available wrench sets in both cases with and without external disturbance are analyzed. The definitions of thrust spaces and wrench spaces in both cases are similar, while the tension spaces are solved in different ways.

The i^{th} UAV's thrust f_i is restricted by the positive minimum thrust $f_{i,min}$ required to maintain itself in the air, and the maximum thrust $f_{i,max}$ that the i^{th} UAV is able to generate. The thrust space $\mathscr{H}$ generalized by a tethered multi-rotor UAVs system with N UAVs is an N-orthotope,

$$\mathscr{H} = \left\{ f \in \mathcal{R}^N : f_{\min} \le f \le f_{\max} \right\} \tag{3}$$

$f = [f_1, \cdots, f_N]^T$, $f_{min} = \left[f_{1,min}, \cdots, f_{N,min}\right]^T$, $f_{max} = \left[f_{1,max}, \cdots, f_{N,max}\right]^T$.

Tension space is the set of tensions that the UAVs can exert on the tethers. Similarly, tension T_i on i^{th} tether is bounded by the positive minimum tension $T_{i,min}$ chosen such that the cable will be tight, and the maximum tension $T_{i,max}$ is the maximum force the i^{th} UAV can exert on the tether which is usually less than the tether's safe operating tension. Accordingly, the tension space can be generalized as:

$$\mathscr{T} = \left\{ T \in \mathcal{R}^N : T_{\min} \le T \le T_{\max} \right\} \tag{4}$$

$T = [T_1, \cdots, T_N]^T$, $T_{min} = \left[T_{1,min}, \cdots, T_{N,min}\right]^T$, $T_{max} = \left[T_{1,max}, \cdots, T_{N,max}\right]^T$. As the tether tensions are supported by UAVs, the maximum tension of each tether will be expressed according to the balance of forces for the i^{th} UAV in Eq. (2).

Case 1 (without external disturbance): With the property of a unit vector, Eq. (2) can be arranged as:

$$\left(m_i\left(\ddot{r}_i - g\right) + T_i q_i\right)^T \left(m_i\left(\ddot{r}_i - g\right) + T_i q_i\right) = f_i^2 \tag{5}$$

Therefore, the explicit relationship between tension and thrust is as follows:

$$T_i^2 - 2T_i m_i q_i^T a_i + m_i^2 a_i^T a_i - f_i^2 = 0 \tag{6}$$

where $a_i = g - \ddot{r}_i$. According to Eq. (6), it is obvious that the maximum available tension can only occur with the maximum UAV thrust. Thus, the maximum tension can be calculated as:

$$T_{i,\max} = m_i a_i^T q_i + \sqrt{f_{i,\max}^2 + m_i^2\left(\left(a_i^T q_i\right)^2 - a_i^T a_i\right)} \tag{7}$$

Considering the quasi-static motion, the maximum tension can be expressed as:

$$T_{i,\max} = m_i g^T q_i + \sqrt{f_{i,\max}^2 + m_i^2 g^2\left(q_{iz}^2 - 1\right)} \tag{8}$$

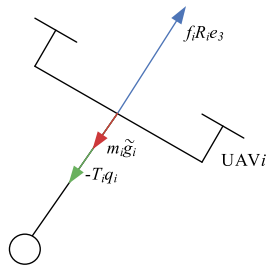

Fig. 2. Force analysis diagram of i^{th} UAV.

where $q_{iz} = [0\ 0\ 1]q_i$.

Case 2 (with external disturbance): When considering with external aerodynamic force, the maximum tension of tether i can be obtained as:

$$T_{i,\max} = m_i \tilde{a}_i^T q_i + \sqrt{f_{i,\max}^2 + m_i^2\left(\left(\tilde{a}_i^T q_i\right)^2 - \tilde{a}_i^T \tilde{a}_i\right)} \tag{9}$$

where $\tilde{a}_i = a_i + \frac{d_i}{m_i}$. Considering the quasi-static motion with $\ddot{r}_i = 0$, the maximum tension of (9) can be rearranged as:

$$T_{i,\max} = m_i \tilde{g}_i^T q_i + \sqrt{f_{i,\max}^2 + m_i^2\left(\left(\tilde{g}_i^T q_i\right)^2 - \tilde{g}_i^T \tilde{g}_i\right)} \tag{10}$$

where $\tilde{g}_i = g + \frac{d_i}{m_i}$. In order to solve the maximum tension force $T_{i,max}$ under disturbance d_i, the following assumption about d_i is made.

Assumption 1. The disturbance d_i acting on UAV i is bounded with $\|d_i/m_i\| \le \tilde{d}_i$, where $\tilde{d}_i$ is a positive scalar.

In reality, it is reasonable to assume that the external disturbance is bounded. The difficulty is that the orientation of disturbance is not sure. To be able to withstand disturbances d_i in any direction, we need to solve the minimum value of $T_{i,max}$. The derivative of $T_{i,max}$ with respect to $\tilde{g}_i$ is obtained as:

$$\frac{\partial T_{i,\max}}{\partial \tilde{g}_i} = m_i q_i + \frac{m_i^2\left(\tilde{g}_i^T q_i\right) q_i - m_i^2 \tilde{g}_i}{\sqrt{f_{i,\max}^2 + m_i^2\left(\left(\tilde{g}_i^T q_i\right)^2 - \tilde{g}_i^T \tilde{g}_i\right)}} \tag{11}$$

When $\partial T_{i,\max}/\partial \tilde{g}_i = 0$, the extremum value of $T_{i,max}$ is obtained. It is obvious that the extremum values of $T_{i,max}$ appear when $\tilde{g}_i$ and q_i are in the same direction or in the opposite direction. According to the schematic diagram of force acting on UAV i as Fig. 2, the minimum value of $T_{i,max}$ is obtained when $\tilde{g}_i$ and q_i are in the opposite direction. Therefore, the minimum value of $T_{i,max}$ is

$$T_{i,\max} = f_{i,\max} - \left\| m_i \tilde{g}_i \right\| \tag{12}$$

After the maximum tension force $T_{i,max}$ is derived, the available wrench set can be solved as the case without disturbance.

Remark 1. In case 1 without external disturbance, the maximum tension force can be calculated with the method in case 2. However, the calculated tension force in case 2 is conservative. Therefore, when the external force is small enough, the tension force can be calculated as case 1.

The available wrench that each tether exerts on the payload can be mapped from tension space $\mathscr{T}$ to wrench space $\mathscr{W}$ with the wrench matrix $W = [q_1, \cdots, q_N]$. Therefore, the wrench space $\mathscr{W}$ satisfies the following relationship:

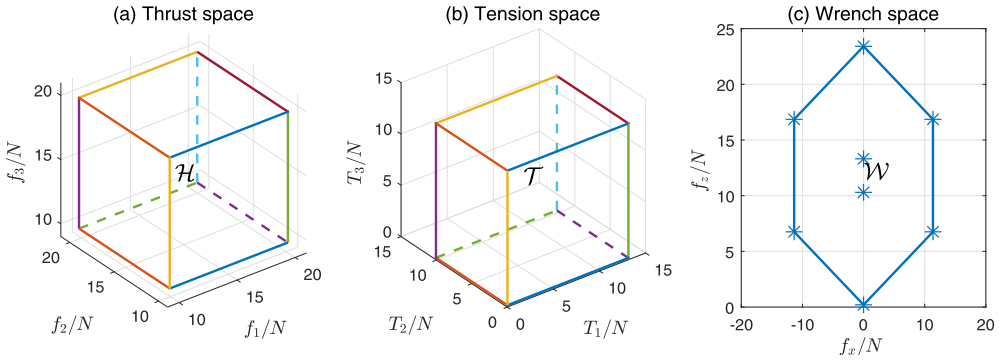

Fig. 3. Thrust $\mathscr{H}$, tension $\mathscr{T}$ and $\mathscr{W}$ spaces in case one.

$$\mathscr{W} = \left\{ w \in \mathcal{R}^d \middle| w = \sum_{i=1}^{N} \alpha_i \Delta T_i q_i + W T_{\min}, 0 \le \alpha_i \le 1 \right\} \tag{13}$$

where w is inside the available wrench set $\mathscr{W}$, d is the dimension of task space, $\Delta T_i = T_{i,\max} - T_{i,\min}$. As the tension space in Eq. (4) is a convex set, the linear mapping of the points bounding the tension space also constructs a convex set. According, the mapping of the vertices of the tension space by the wrench matrix in Eq. (13) fully contains all feasible wrenches. Therefore, the available wrench set of the payload can be expressed as a convex hull of the set of d-dimensional points W_a.

$$W_a = W diag(\Delta T)\alpha + W T_{\min} \mathbf{1}_{(1,2^N)} \tag{14}$$

where $\mathbf{1}_{(1,2^N)}$ is a row vector of ones with 2^N columns, $diag(*)$ is a diagonal matrix with vector $*$ as the main diagonal elements, the matrix α is the set of all combinations of tension limits bounding the tension space.

2.3. Configuration analysis

According to Eqs. (7), (12) and (13), the available wrench set $\mathscr{W}$ is related to the minimum tension, acceleration of UAVs, maximum thrust of UAVs, external disturbance and the configuration of tethers. The robustness of the available wrench set is evaluated by capacity margin γ. It is defined as the shortest distance from the $-m_p g$ to the nearest facet of $\mathscr{W}$. Based on force balance analysis of payload, the wrench space produced by the tension force is used to resist other active forces (e.g. external aerodynamic force) and inertia force acting on payload. With the idea of Chebychev ball, the capacity margin can be easily found by solving the following linear optimization problem. First, we need to rearrange the wrench space $\mathscr{W}$ to a standard form of polytope. The wrench space in (13) can be rewritten as:

$$\omega = W \Delta T \alpha + W T_{\min} \tag{15}$$

where ΔT and α are diagonal matrices with ΔT_i and α_i being the diagonal elements. With $0 \le \alpha_i \le 1$, we have

$$A_\alpha \alpha \le b_\alpha \tag{16}$$

where $A_\alpha = \begin{bmatrix} 1 & 0 & \cdots & 0 \\ -1 & 0 & \cdots & 0 \\ \vdots & \vdots & \ddots & \vdots \\ 0 & 0 & \cdots & 1 \\ 0 & 0 & \cdots & -1 \end{bmatrix}$ $b_\alpha = \begin{bmatrix} 1 \\ 0 \\ \vdots \\ 1 \\ 0 \end{bmatrix}$.

Considering the linear map (15), the polyhedron of the available wrench set is

$$A_\alpha (W\Delta T)^+ \omega \le A_\alpha (W\Delta T)^+ W T_{\min} + b_\alpha \tag{17}$$

where $(\cdot)^+$ represents the Moore-Penrose inverse of matrix. For simplicity, we have $A_\omega = A_\alpha (W\Delta T)^+$ and $b_\omega = A_\alpha (W\Delta T)^+ W T_{\min} + b_\alpha$. With the idea of Chebychev ball, the capacity margin is obtained by solving the following linear optimization problem

$$\begin{aligned} &\max\ R \\ &subj.\ to\ \{A_\omega\}_i x_c + R\|\{A_\omega\}_i\|_2 \le \{b_\omega\}_i \end{aligned} \tag{18}$$

where $\{A_\omega\}_i$ and $\{b_\omega\}_i$ are the i^{th} row of A_ω and b_ω, respectively; $x_c = -m_p g$. With the definition of capacity margin, we have $\gamma = R$. The maximum available acceleration of payload is analyzed in the subsequent part. According to force balance analysis of payload, it is obvious that $\omega = m_p \ddot{r}_p - m_p g$. The maximum available acceleration of payload is obtained by solving the following linear optimization problem

$$\begin{aligned} &\max\ \left\| m_p \ddot{r}_p \right\| \\ &subj.\ to\ \{A_\omega\}_i \left(m_p \ddot{r}_p - m_p g \right) \le \{b_\omega\}_i \end{aligned} \tag{19}$$

To be able to generate acceleration in any direction, the linear optimization in (19) should be improved as

$$\begin{aligned} &\max\ \left\| m_p \ddot{r}_p \right\| \\ &subj.\ to\ \|\{A_\omega\}_i\|_2 \left\| m_p \ddot{r}_p \right\| - \{A_\omega\}_i m_p g \le \{b_\omega\}_i \end{aligned} \tag{20}$$

According to above linear optimization problems in (18) and (20), we have

$$\gamma = \max \left\| m_p \ddot{r}_p \right\| \tag{21}$$

Therefore, the capacity margin is used to evaluate the available maximum acceleration of the payload.

In the following, the relationship between the configuration of tethers and the available wrench set is discussed.

Case one: a planar tethered multi-rotor UAVs system composed of three UAVs with a single tether each attached to a point mass will be considered. It has the configuration $\mathscr{C} = [\theta_1, \theta_2, \theta_3] = [\pi/6\,, \pi/2\,, 5\pi/6\,]$ rad. The UAVs have a mass of $m_i = 1$ kg and maximum thrust of $f_{i,max} = 20$ N.

Case two: a tethered multi-rotor UAVs system in the three dimensional space is composed of three UAVs with a single tether each attached to a point mass. It has the configuration $\mathscr{C}_1 = [\theta_1, \theta_2, \theta_3] = [\pi/3\,, \pi/3\,, \pi/3\,]$ rad and $\mathscr{C}_2 = [\gamma_1, \gamma_2, \gamma_3] = [0\,, 2\pi/3\,, -2\pi/3\,]$ rad. The parameters of UAVs are chosen as case one.

From Figs. 3 and 4, it is shown that the wrench spaces are distinctly different between case one and case two, in spite of the identical UAVs. The configuration of tethers is one of the major

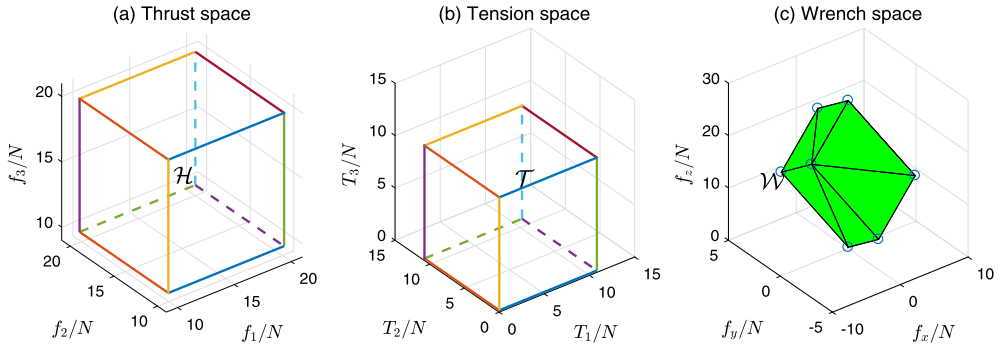

Fig. 4. Thrust $\mathscr{H}$, tension $\mathscr{T}$ and $\mathscr{W}$ spaces in case two.

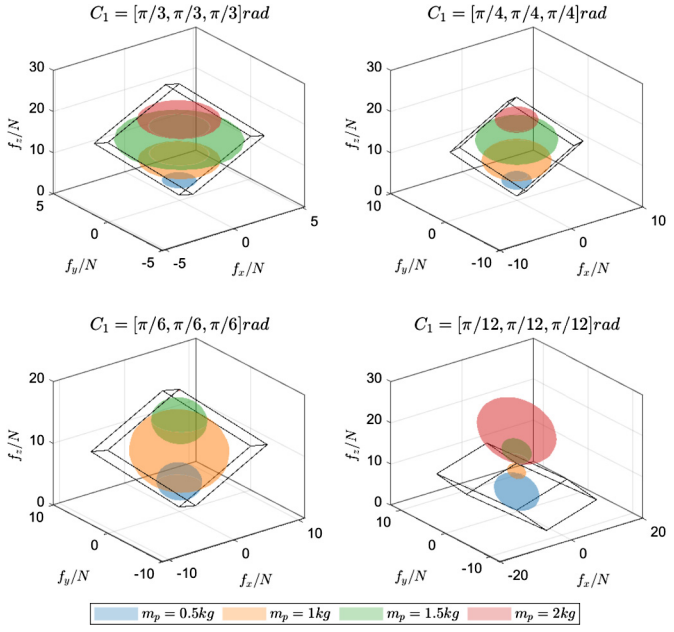

Fig. 5. The available wrench space $\mathscr{W}$ is depicted as hexahedron in each subgraph, the ball is with $-m_p g$ as the center and γ as the radius. (For interpretation of the colors in the figure(s), the reader is referred to the web version of this article.)

factors which affect the available wrench space. The three dimensional system in case two is further discussed with different configurations $\mathscr{C}_1$ and payload mass m_p.

Case three: The parameters of tethered multi-rotor UAVs system in this case are same as case two, except configurations $\mathscr{C}_1$ and payload mass m_p. The available wrench space and robustness of tethered multi-rotor UAVs system are analyzed in different scenes with payload mass $m_p = 0.5, 1, 1.5, 2$ kg and configurations with $\mathscr{C}_1 = [\pi/3\,, \pi/3\,, \pi/3\,]$ rad, $\mathscr{C}_1 = [\pi/4\,, \pi/4\,, \pi/4\,]$ rad, $\mathscr{C}_1 = [\pi/6\,, \pi/6\,, \pi/6\,]$ rad and $\mathscr{C}_1 = [\pi/12\,, \pi/12\,, \pi/12\,]$ rad.

In Fig. 5, the available wrench sets of the tethered multi-rotor UAVs system for different payload masses and configurations are shown. The four spheres in each subgraph are centered at $-m_p g$ with payload masses $0.5, 1, 1.5, 2$ kg respectively and have radius corresponding to the magnitude of the distance from the $-m_p g$ to the nearest facet of $\mathscr{W}$. From left to right in Fig. 5, the angles of configuration $\mathscr{C}_1$ get smaller which means UAVs bloom the formation by flying away from each other. As we know, a tethered multi-rotor UAVs system with UAVs shrinking toward each other can suspend heavier payload, while the stiffness of a tethered multi-rotor UAVs system gets stronger with UAVs bloom away from each other. Therefore, it is reasonable that the available wrench set becomes chunky with the angels of configuration $\mathscr{C}_1$ get smaller. Simultaneously, the spheres will escape from the available wrench space when the payload is too heavy and the formation of UAVs bloom away from each other. It can be derived that the configuration of UAVs has a significant influence on the robustness of payload transportation. On the one hand, the blooming configuration of UAVs will improve the robustness of payload to counteract the environment disturbances. On the other hand, the maximum payload a tethered multi-rotor UAVs system with blooming configuration suspends is lighter.

The relationship between capacity margin γ and inclination angle θ (angle from z_0 to the tether) is shown in Fig. 7. The solid line represents the relationship between capacity margin and inclination angle with different payload mass. The dotted line represents the inclination angle with capacity margin being 0, which is the maximum allowable angle under the corresponding mass. In Fig. 8, the evolution of maximum capacity margin and the corresponding best inclination angle with different payload mass are depicted. It is obvious that with the increasement of mass of payload, the best inclination angle of the configuration is becoming smaller. However, the capacity margin is not monotonic to the mass of payload. We can choose the optimal configuration (the inclination angle) with a given payload at which the maximum capacity margin occurs.

Case four: To demonstrate the relevance between the capacity margin and the motion acceleration in dynamical situation, the geometric relationship between available wrench space and stable ball is carefully studied by gradually increasing the motion acceleration and the weight of the payload. With a bigger stable ball wrapped in the wrench space, there is more sufficient room for high maneuverability. From Fig. 6, it can be derived that the upper limit of payload weight that the system can manipulate gets smaller and smaller with the acceleration increasing.

3. Trajectory generation

Assume to have a desired feasible payload trajectory r_{pd}, derived from a planner or a human pilot, which fulfills the available wrench set and positive capacity margin constraints. There are many existing novel results about solving the problem of feasible optimal trajectory (e.g., [26], [27], [39]), which can be used to optimize the trajectory of payload. How can the payload track the desired trajectory by controlling the UAVs? To tackle this problem, a tension distribution algorithm is proposed to optimize the desired trajectories of UAVs.

From Eq. (1), the desired wrench applied to the payload for desired payload trajectory tracking in task space is calculated as:

$$\omega_p = m_p \ddot{r}_{pd} - m_p g \tag{22}$$

For a tethered multi-rotor UAVs system, the payload can only be controlled passively through the tethers. The desired wrench ω_p is only provided by the connected tethers which is organized as:

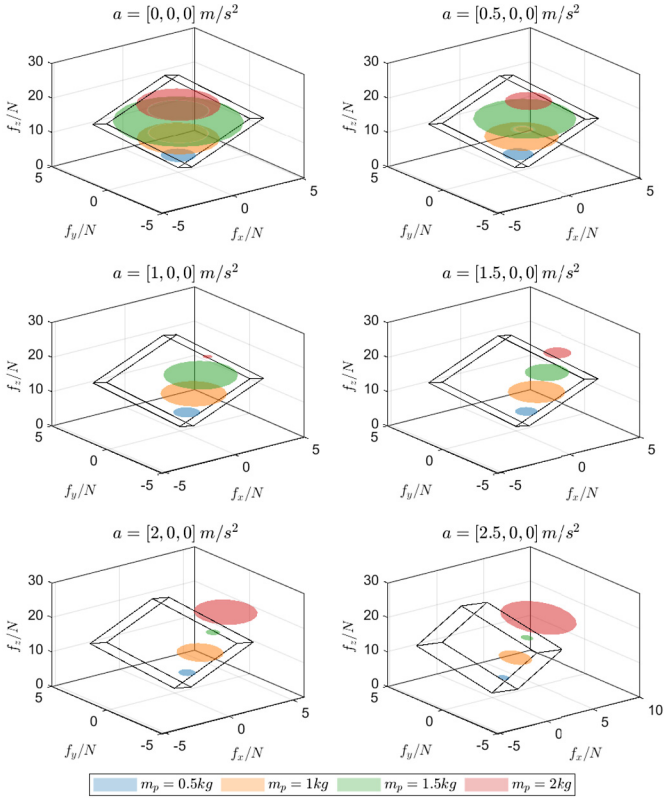

Fig. 6. The relationship between available wrench spaces $\mathscr{W}$ and ball spaces with different accelerations in case four.

$$\omega_p = WT \tag{23}$$

The expression in Eq. (23) is an under-determined set of equations. Although, it can be computed by inverting the matrix. However, the solution may be invalid recalling Eq. (4) that the tensions must be positive and have a maximum value. Our method generates an optimal tension distribution that minimizes the cable tensions while respecting to the tension constraint (23) and collision avoidance between UAVs. We are interested in finding tension distribution that minimize the total tension which will reduce interference with UAVs. The optimization program to solve this problem is specified as follows:

$$\min \|WT\| \tag{24}$$

$$s.t. \begin{cases} WT - \omega_p = 0 \\ \frac{q_i^T q_j}{\|q_i\|\|q_j\|} - \cos\beta \le 0, & \{i, j \,|\{1, \cdots, N\}, i \ne j\} \\ T_i - T_{i,\max} < 0, & \{i \,|\{1, \cdots, N\}\} \\ T_{i,\min} - T_i < 0, & \{i \,|\{1, \cdots, N\}\} \end{cases}$$

where β is the minimum angle between two tethers allowed for collision avoidance between UAVs. The sequential least squares programming is used to solve the optimization problem.

4. Dynamics and control

4.1. System dynamics

The translational dynamics of a multi-rotor UAV can be modeled as Eq. (2), where the rotation matrix R_i is defined as:

$$R_i = \begin{bmatrix} c\phi_i c\psi_i & s\phi_i s\theta_i c\psi_i & c\phi_i s\theta_i c\psi_i + s\phi_i s\psi_i \\ c\theta_i s\psi_i & s\phi_i s\theta_i s\psi_i & c\phi_i s\theta_i s\psi_i - s\phi_i c\psi_i \\ -s\theta_i & s\phi_i c\theta_i & c\phi_i c\theta_i \end{bmatrix} \tag{25}$$

where the shorthands $s\phi$ and $c\phi$ represent $\sin\phi$ and $\cos\phi$ for simplicity respectively, ϕ_i, θ_i and ψ_i are roll, pitch and yaw angle of the i^{th} UAV respectively. The tethers are assumed to attach to the center of mass of each multi-rotor UAV such that the rotational dynamics is decoupled from the rest of the system. Therefore, the rotational dynamics of the i^{th} UAV is shown as:

$$\begin{cases} \ddot{\phi}_i = \left(l_\phi u_{2i} + \dot{\theta}_i\dot{\psi}_i\left(I_{y_i} - I_{z_i}\right)\right)/I_{x_i} \\ \ddot{\theta}_i = \left(l_\theta u_{3i} + \dot{\phi}_i\dot{\psi}_i\left(I_{z_i} - I_{x_i}\right)\right)/I_{y_i} \\ \ddot{\psi}_i = \left(u_{4i} + \dot{\phi}_i\dot{\theta}_i\left(I_{x_i} - I_{y_i}\right)\right)/I_{z_i} \end{cases} \tag{26}$$

where l_ϕ and l_θ represent the half of roll and pitch motor-to-motor distances, respectively; u_{2i}, u_{3i} and u_{4i} are three independent inputs for the attitude control of the i^{th} UAV; I_{x_i}, I_{y_i} and I_{z_i} are the rotational inertia. In Eq. (2), $u_i = f_i R_i e_3$ is a virtual control input to a low-level attitude controller. According to Eqs. (2) and (25), the relationship between virtual control u_i and thrust f_i, roll angle ϕ_i, pitch angle θ_i is derived as:

$$\begin{cases} f_{i,d} = u_{z_i}/\cos\phi_{i,d}\cos\theta_{i,d} \\ \theta_{i,d} = \arctan\left(\left(u_{x_i}\cos\psi_{i,d} + u_{y_i}\sin\psi_{i,d}\right)/u_{z_i}\right) \\ \phi_{i,d} = \arctan\left(\left(u_{x_i}\sin\psi_{i,d} - u_{y_i}\cos\psi_{i,d}\right)\cos\theta_{i,d}/u_{z_i}\right) \end{cases} \tag{27}$$

where $f_{i,d}$, $\phi_{i,d}$, $\theta_{i,d}$ and $\psi_{i,d}$ are desired values of f_i, ϕ_i, θ_i and ψ_i respectively; $u_i = \left[u_{x_i}, u_{y_i}, u_{z_i}\right]^T$.

For a tethered multi-rotor UAVs system, the multiple UAVs are connected to the same payload. Consequently, the tension force $T_i q_i$ in Eqs. (1) and (2) is a highly dynamic function with the motion interactions of the multibody in the system. Further to develop the transportation simulation, the tension forces can be calculated with the Udwadia-Kalaba equation. The tension forces are a function of the states of all involved bodies, and are thus most suited for simulation purposes.

A constraint on the i^{th} UAV and payload is imposed by the cable i, which has the following form

$$\left\|r_{p,i}\right\|^2 - L_i^2 = 0 \tag{28}$$

where $r_{p,i} = r_i - r_p$ and L_i is the nominal length of the i^{th} cable. Double differential Eq. (28) can get the expression

$$A_i\ddot{r} = b_i \tag{29}$$

$A_i = 2r_{p,i}^T\left[0_{3\times3(i-1)}\ I_{3\times3}\ 0_{3\times3(N-i)}\ -I_{3\times3}\right] \in \mathcal{R}^{1\times3(N+1)}$, $r = \left[r_1^T, \cdots, r_N^T, r_p^T\right]^T$, $b_i = -2\dot{r}_{p,i}^T\dot{r}_{p,i}$. Then, the total tension force $\mathcal{T}$ of the tethers can be expressed as:

$$\mathcal{T} = (M \otimes I_3)^{1/2}\left(A(M \otimes I_3)^{-1/2}\right)^+(b - A\ddot{r}) \tag{30}$$

$\mathcal{T} = \left[T_1 q_1^T, \cdots, T_N q_N^T, \sum_{i=1}^N T_i q_i^T\right]^T \in \mathcal{R}^{3(N+1)\times1}$, $M = diag\left[m_1, \cdots, m_N, m_p\right] \in \mathcal{R}^{(N+1)\times(N+1)}$, $A = \left[A_1^T, \cdots, A_N^T\right]^T \in \mathcal{R}^{N\times3(N+1)}$, $b = \left[b_1^T, \cdots, b_N^T\right]^T \in \mathcal{R}^{N\times1}$, $\otimes$ denotes the Kronecker product and $(*)^+$ denotes the Moore-Penrose pseudo inverse. However, because of numerical integration error, constraints on velocity and position are not equal to zero, i.e.,

$$\begin{cases} \Delta\dot{r}_{p,i} \ne 0 \\ \Delta r_{p,i} \ne 0 \end{cases} \tag{31}$$

where $\Delta r_{p,i} = \left\|r_{p,i}\right\|^2 - L_i^2$. This means that the error may grow unlimited. It depends on the integration method used and the step size. Therefore, it is necessary to avoid unbounded growing of the error with some suitable methods. The Baumgarte method is a simple state feedback approach to add two variables to this system as,

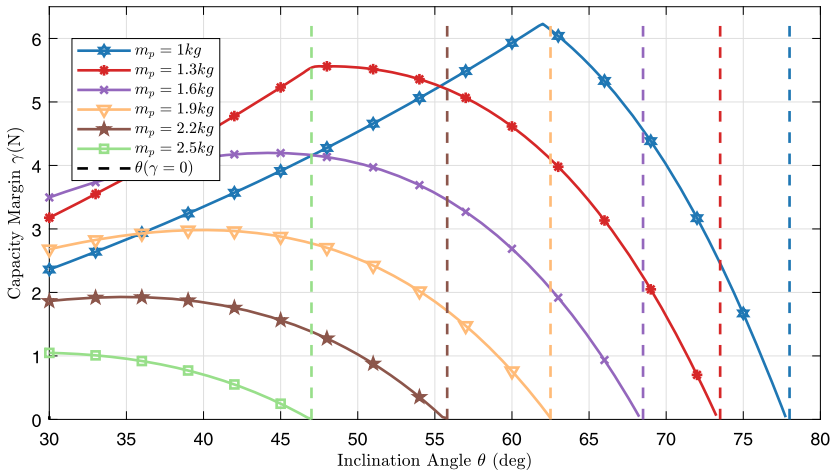

Fig. 7. The capacity margin γ.

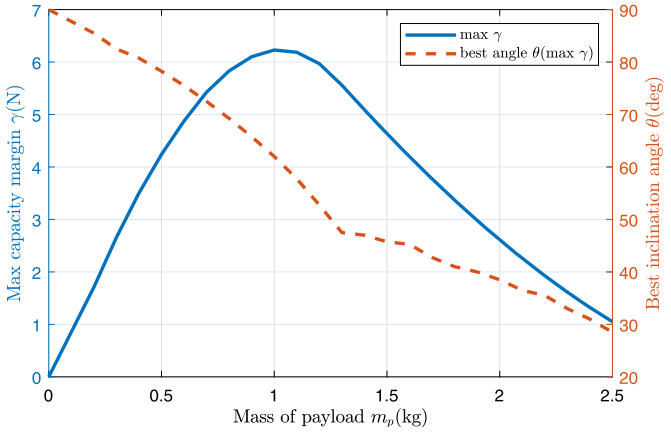

Fig. 8. The maximum capacity margin γ and the corresponding inclination angle θ with different payload mass m_p.

$$\Delta\ddot{r}_{p,i} = -2\alpha\Delta\dot{r}_{p,i} - \beta^2\Delta r_{p,i} \tag{32}$$

where α and β are feedback gains. This method has been used to handle the numerical integration error in [28]. By substituting (32) in the tension equation (30), it can be rewritten as

$$\mathcal{T} = \bar{M}^{1/2}\left(A\bar{M}^{-1/2}\right)^{+}\left(b - 2\alpha\Delta\dot{r}_p - \beta^2\Delta r_p - A\ddot{r}\right) \tag{33}$$

where $\bar{M} = M \otimes I_3$, $\Delta\dot{r}_p = \left[\Delta\dot{r}_{p,1}, \cdots, \Delta\dot{r}_{p,N}\right]^T$ and $\Delta r_p = \left[\Delta r_{p,1}, \cdots, \Delta r_{p,N}\right]^T$. Eq. (33) can be used to instead of the tension in Eq. (30) in numerical simulations. It ensures that the error on the constraints can not grow unbounded. In the following controller design, the explicit tension forces are unknown without force measurement device.

4.2. Controller design

Our control objective is to design f_i, u_{2i}, u_{3i} and u_{4i} in a decentralized way such that the UAVs converge to the generated trajectories, while the payload is passively regulated to the desired trajectory. The control of an UAV has a cascade structure. The outer loop is firstly designed as a virtual trajectory tracking controller which drives the payload's and the multi-rotor UAVs' translational motion along a desired trajectory. The inner loop is the attitude control to point the actual lift to the reference direction obtained by the outer loop. The dynamics of i^{th} UAV in Eq. (2) can be further arranged as

$$\ddot{r}_i = u_i + \xi_i \tag{34}$$

where $u_i = f_i R_i e_3/m_i + g$, $\xi_i = -T_i q_i/m_i + d_i/m_i$. The fixed-time control with strong robustness and fast convergence has been generalized to UAVs stabilization control problem [29]. In the following, a fixed-time observer is designed. The more details about fixed-time convergence can be found in [30–32]. A fixed-time ESO is designed as:

$$\begin{cases} \dot{\hat{x}}_i = \hat{v}_i - \gamma_{11}\theta sig^{\alpha_{11}}(e_{i1}) - \gamma_{12}(1-\theta)\, sig^{\alpha_{12}}(e_{i1}) \\ \dot{\hat{v}}_i = u_i + \hat{\xi}_i - \gamma_{21}\theta sig^{\alpha_{21}}(e_{i1}) - \gamma_{22}(1-\theta)\, sig^{\alpha_{22}}(e_{i1}) \\ \dot{\hat{\xi}}_i = -\gamma_{31}\theta sign(e_{i1}) - \gamma_{32}(1-\theta)\, sig^{\alpha_{32}}(e_{i1}) \end{cases} \tag{35}$$

where $e_{i1} = \hat{x}_i - r_i$, $\hat{x}_i$, $\hat{v}_i$ and $\hat{d}_i$ are estimations of r_i, $\dot{r}_i$ and d_i respectively; γ_{ij}, $i = 1, 2, 3$, $j = 1, 2$ are positive constants, the parameters γ_{ij} can be selected based on the gains for the recursive high-order sliding mode differentiator, which are chosen as $\gamma_{11} = 2\bar{\xi}^{1/3}$, $\gamma_{21} = 1.5\sqrt{2}\bar{\xi}^{1/2+1/6}$, $\gamma_{31} = 1.1\bar{\xi}$, where $\|\dot{\xi}_i\| \le \bar{\xi}$, see reference [33], $\alpha_{11} = \frac{2}{3}$, $\alpha_{21} = \frac{1}{3}$, $\alpha_{i2} = \frac{3+\alpha i}{3}$, where α is sufficiently small positive scalar. The parameter θ is selected as $\theta = 0$ when $t \le t_u$, otherwise $\theta = 1$, where t_u is some arbitrarily chosen positive parameter. Lastly, the parameters γ_{i2} should satisfy the following condition, that the matrix $\mathcal{A}$ defined as

$$\mathcal{A} = \begin{bmatrix} -\gamma_{12} & 1 & 0 \\ -\gamma_{22} & 0 & 1 \\ -\gamma_{32} & 0 & 0 \end{bmatrix} \tag{36}$$

is Hurwitz.

With the observer in Eq. (35), the fixed-time ESO based output feedback position tracking controller is designed as:

$$u_i = \ddot{r}_{id} - k_1\left(\hat{v}_i - \dot{r}_{id}\right) - k_2\left(r_i - r_{id}\right) - \hat{\xi}_i \tag{37}$$

where r_{id} is the desired trajectory of the i^{th} UAV, $r_{id} = r_{pd} + L_i q_i$; $\dot{r}_{id}$ and $\ddot{r}_{id}$ are the first and second derivatives of r_{id} with respect to time respectively; k_1 and k_2 are feedback gains to be designed.

For the inner loop controller design, the desired yaw angle of the i^{th} UAV is $\psi_i = 0$. The attitude controller is designed as:

$$\begin{cases} u_{2i} = \left(-\dot{\phi}_i\dot{\psi}_i\left(I_{y_i} - I_{z_i}\right) + I_{x_i}\left(\ddot{\phi}_{i,d} - k_{31}\dot{e}_{\phi_i} - k_{41}e_{\phi_i}\right)\right)/l_i \\ u_{3i} = \left(-\dot{\phi}_i\dot{\psi}_i\left(I_{z_i} - I_{x_i}\right) + I_{y_i}\left(\ddot{\theta}_{i,d} - k_{32}\dot{e}_{\theta_i} - k_{42}e_{\theta_i}\right)\right)/l_i \\ u_{4i} = -\dot{\phi}_i\dot{\theta}_i\left(I_{x_i} - I_{y_i}\right) + I_{z_i}\left(\ddot{\psi}_{i,d} - k_{33}\dot{e}_{\psi_i} - k_{43}e_{\psi_i}\right) \end{cases} \tag{38}$$

where $e_{\phi_i} = \phi_i - \phi_{i,d}$, $e_{\theta_i} = \theta_i - \theta_{i,d}$, $e_{\psi_i} = \psi_i - \psi_{i,d}$, k_{3i} and k_{4i}, $i = 1, 2, 3$ are feedback gains.

Remark 2. Most existing results on UAVs controller design suffer from the lack of stability analysis of the closed-loop system. They always suppose that the inner loop is stable and the bandwidth of the inner loop is significantly higher than that of the outer loop. Therefore, the controller design and stability analysis of outer loop are largely independent of the inner loop. The dynamics model of rotorcraft UAVs is composed of two cascaded subsystems that are coupled by a nonlinear interconnection term. The stability proof of the closed-loop system is implemented with the method proposed in [35].

Theorem 1. *The observer states $\hat{x}_i$, $\hat{v}_i$ and $\hat{\xi}_i$ in Eq. (35) converge to r_i, $\dot{r}_i$ and ξ_i within globally finite time T_{EO}. Furthermore, the states in Eq. (34) under the fixed-time ESO (35) do not escape during the finite interval $t \in [0, T_{EO}]$, which is necessary to derive the following conclusion. With the fixed-time ESO based output feedback controller (37) and attitude controller (38), the closed-loop system in cascade composed of (34) and (26) is asymptotically stable. Therefore, the system will asymptotically converge to the desired trajectory.*

Proof. First, the globally finite time convergence of the ESO (35) will be discussed. Define the observer estimation errors

$$\begin{cases} e_{i1} = \hat{x}_i - r_i \\ e_{i2} = \hat{v}_i - \dot{r}_i \\ e_{i3} = \hat{\xi}_i - \xi_i \end{cases} \tag{39}$$

The derivative of (39) can be described as

$$\begin{cases} \dot{e}_{i1} = e_{i2} - \gamma_{11}\theta sig^{\alpha_{11}}(e_{i1}) - \gamma_{12}(1-\theta)\, sig^{\alpha_{12}}(e_{i1}) \\ \dot{e}_{i2} = e_{i3} - \gamma_{21}\theta sig^{\alpha_{21}}(e_{i1}) - \gamma_{22}(1-\theta)\, sig^{\alpha_{22}}(e_{i1}) \\ \dot{e}_{i3} = -\gamma_{31}\theta sign(e_{i1}) - \gamma_{32}(1-\theta)\, sig^{\alpha_{32}}(e_{i1}) - \dot{\xi}_i \end{cases} \tag{40}$$

According to Theorem 1 in [34], the error system (40) is uniformly finite-time convergence, i.e., $\hat{x}_i = r_i$, $\hat{v}_i = \dot{r}_i$ and $\hat{\xi}_i = \xi_i$ after bounded convergence time T_{EO}. Then, we prove the boundedness of the states in dynamics (34) during the time interval $t \in [0, T_{EO}]$. The candidate function for system (34) is chosen as $V = e_i^T e_i/2 + \dot{e}_i^T \dot{e}_i/2$, where e_i=$r_i - r_{id}$ and $\dot{e}_i$=$\dot{r}_i - \dot{r}_{id}$. The derivative of V is

$$\begin{aligned} \dot{V} &= e_i^T \dot{e}_i + \dot{e}_i^T \ddot{e}_i \\ &= e_i^T \dot{e}_i + \dot{e}_i^T \left(-k_1(\hat{v}_i - \dot{r}_{id}) - k_2(r_i - r_{id}) - \hat{\xi}_i + \xi_i\right) \\ &\le (1+k_2)\|e_i\|^2/2 + (2+3k_1+k_2)\|\dot{e}_i\|^2/2 \\ &\quad + \|e_{i3}\|^2/2 + k_1\|e_{i2}\|^2 \\ &\le kV + c \end{aligned} \tag{41}$$

where $k = 2 + 3k_1 + k_2$, $c = \|e_{i3}\|^2/2 + k_1\|e_{i2}\|^2$. According to previous analysis, e_{i2} and e_{i3} are bounded. Then, we have

$$V \le (V(0) + c/k)\, e^{kt} - c/k \tag{42}$$

As we can see, when $t \in [0, T_{EO}]$, the states in dynamics (34) are bounded with the bounded initial value $V(0)$. Therefore, the states in Eq. (34) under the fixed-time ESO (35) do not escape during the finite time interval $t \in [0, T_{EO}]$. Being similar to [35], the closed-loop system stability is analyzed according to the following three steps.

1) Firstly, it should be guaranteed that the system (34) is globally exponentially stable without considering the interconnection with inner loop.

After $t \ge T_{EO}$, the feedback controller (37) is arranged as $u_i = \ddot{r}_{id} - k_1(\dot{r}_i - \dot{r}_{id}) - k_2(r_i - r_{id}) - \xi_i$. The closed loop system is $\ddot{e}_i + k_1\dot{e}_i + k_2 e_i = 0$. With $k_1 > 0$ and $k_2 > 0$, we can conclude that the system (34) is globally exponentially stable. The global exponential stability of the outer loop subsystem implies that there exist a positive definite radially unbounded function $V(\chi)$ and positive constants ε_1 and ε_2 where $\chi = [e_i; \dot{e}_i]$ such that, for $\|\chi\| \ge \varepsilon_1$, $\dot{V} \le 0$ and $\left\|\frac{\partial V}{\partial \chi}\right\| \|\chi\| \le \varepsilon_2 V(\chi)$.

2) Secondly, the inner loop system is globally exponentially stable with the designed controller (38).

According to (26) and (38), the closed-loop system of the inner loop is rearranged as:

$$\begin{cases} \ddot{e}_{\phi_i} = -k_{31}\dot{e}_{\phi_i} - k_{41}e_{\phi_i} \\ \ddot{e}_{\theta_i} = -k_{32}\dot{e}_{\theta_i} - k_{42}e_{\theta_i} \\ \ddot{e}_{\psi_i} = -k_{33}\dot{e}_{\psi_i} - k_{43}e_{\psi_i} \end{cases} \tag{43}$$

It is obvious that the closed-loop system (43) is globally exponentially stable with parameters k_{3i} and k_{4i}, $i = 1, 2, 3$ being positive scalars.

3) Thirdly, we should prove that the interconnection term satisfies growth condition defined in Theorem 2 in [35].

As derived in [35], the interconnection term Δ_i is obtained as $\Delta_i = \frac{1}{m_i} f_i H_i$, where H_i is a nonlinear function related to desired attitudes and attitude tracking errors. The norm of the interconnection term Δ_i can be derived as:

$$\|\Delta_i\| = \frac{1}{m_i} f_i \|H_i\| = \frac{1}{m_i} f_i \sqrt{h_{x_i}^2 + h_{y_i}^2 + h_{z_i}^2} \tag{44}$$

where $H_i = [h_{x_i}; h_{y_i}; h_{z_i}]$, $f_i = m_i\|u_i - g\| = m_i\sqrt{u_{ix}^2 + u_{iy}^2 + (u_{iz}+g)^2}$. Before proving the growth condition of interconnection term Δ_i, the following two Lemmas are needed.

Lemma 1. *The desired trajectory r_{id} and its first and second derivatives are bounded. Then, with the designed outer loop controller (37), we can derive that there exist positive constants ε and μ_1 such that the thrust force f_i satisfies the following inequality:*

$$f_i \le \begin{cases} \mu_1\|\chi\| & \|\chi\| \ge \varepsilon \\ \mu_1\varepsilon & \|\chi\| < \varepsilon \end{cases} \tag{45}$$

Lemma 2. *According to [35], the interconnection term H_i satisfies the following property: $\|H_i\| \le \mu_2\|e_\eta\|$, where μ_2 is positive constant and $e_\eta = [e_\phi, e_\theta, e_\psi]$.*

According to Lemma 1 and 2, for $\|\chi\| \ge \varepsilon$, it can be derived that

$$f_i\|H_i\| \le \mu_1\mu_2\|\chi\|\|e_\eta\| \tag{46}$$

Finally, the interconnection term satisfies the following inequality:

$$\|\Delta_i\| = \frac{1}{m_i} f_i\|H_i\| \le \gamma(\|e_\eta\|)\|\chi\|, \quad for\ \|\chi\| \ge \varepsilon \tag{47}$$

where $\gamma(\|e_\eta\|) = \frac{1}{m_i}\mu_1\mu_2\|e_\eta\|$ is a class-$\mathcal{K}$ function. Therefore, the interconnection term satisfies the growth condition. According to 1), 2) and 3), the global asymptotic stability of the closed-loop system is proved.

Remark 3. An easy-to-implement output feedback control is designed. The event-triggered control algorithm has been received considerable investigation with its irreplaceable advantages compared with time-triggered control [36–38]. Further, to reduce the computational burden and energy consumption, we will try to use it in tethered multi-rotor UAVs.

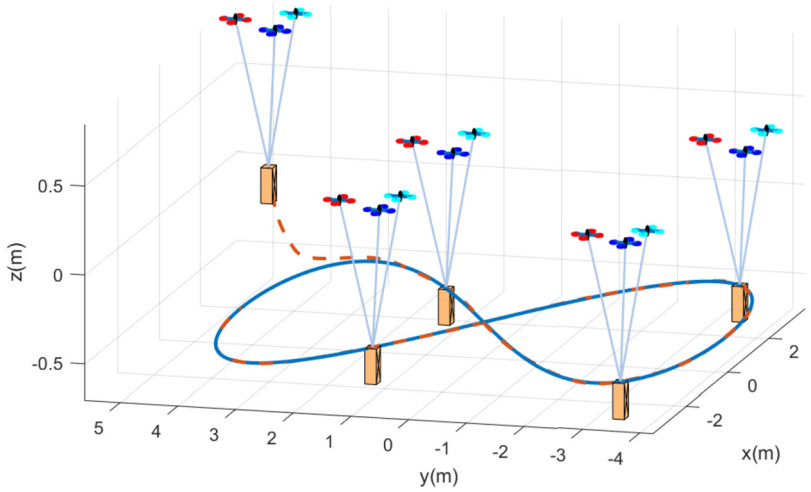

Fig. 9. 3D view of the tethered multi-rotor UAVs system.

5. Simulation study

As an example to validate the designed controller, consider the configuration with $N = 3$ UAVs carrying the suspended load. Each UAV has a mass $m_i = 1$ kg, and the payload has mass $m_p = 0.5$ kg connected with tethers of length $L_i = 1$ m. The desired trajectory of the payload is chosen as $r_{pd} = [3\sin(0.1\pi t); 4.2\cos(0.05\pi t); -0.5]$ m, which is a figure-eight curve like an ∞ symbol. The desired trajectory of quadrotor is generated according to Eq. (24). The initial position of payload is $r_{p0} = [3; 4.8; 0]$ m, and the initial unit vectors of three tethers are $q_{10} = \left[0; 1/\sqrt{3}; \sqrt{2}/\sqrt{3}\right]$, $q_{20} = \left[-1/2; -1/\left(2\sqrt{3}\right); \sqrt{2}/\sqrt{3}\right]$, $q_{30} = \left[1/2; -1/\left(2\sqrt{3}\right); \sqrt{2}/\sqrt{3}\right]$. The inertia is $J_i = diag\left(I_{x_i}, I_{y_i}, I_{z_i}\right)$, where $I_{x_i} = 3.32 * 10^{-3}$ kg m^2, $I_{y_i} = 3.32 * 10^{-3}$ kg m^2, $I_{z_i} = 5 * 10^{-3}$ kg m^2. The distance between the center of the rotor and the origin of the body frame is $l_i = 0.15$ m. The maximum thrust $f_{i,max}$ that the i^{th} UAV is able to generate is 20 N. The controller parameters are selected as follows: $k_1 = 1$, $k_2 = 2$, $k_3 = 1$, $k_4 = 1$. The observer parameters are selected as: $\gamma_{11} = 5$, $\gamma_{21} = 20$, $\gamma_{31} = 50$, $\gamma_{12} = 5$, $\gamma_{22} = 20$, $\gamma_{32} = 50$, $\alpha_{11} = 0.9$, $\alpha_{12} = 1.1$, $\gamma = 0.01$.

A three dimensional view of a tethered multi-rotor UAVs system is presented in Fig. 9, where three UAVs cooperatively manipulate the payload suspended by three tethers from the UAVs. The payload can passively track the desired trajectory only by controlling UAVs to fly along the designed trajectory in (24) under the proposed controller without the payload's states feedback. Simultaneously, collision between UAVs would be avoided when flying along the designed trajectory. The payload trajectory tracking errors are shown in Fig. 10. It is obvious that the tracking errors converge to a small domain around the desired trajectory which validates the effectiveness of the proposed trajectory generation method in (24) and controller in (37). The tension on each UAV is depicted in Fig. 11. Under the designed fixed-time extended state observer in (35), the actual tension on each UAV would be immediately and accurately estimated. With the designed observer, only the position feedback of UAVs is required to construct the controller. Therefore, the observer can effectively compensate the disturbances on UAVs while simplifying the realization of the controller. The thrust development of each UAV is shown on Fig. 12. It is continuous and satisfies the maximum thrust constraint. Accordingly, the controller designed in this paper is realizable.

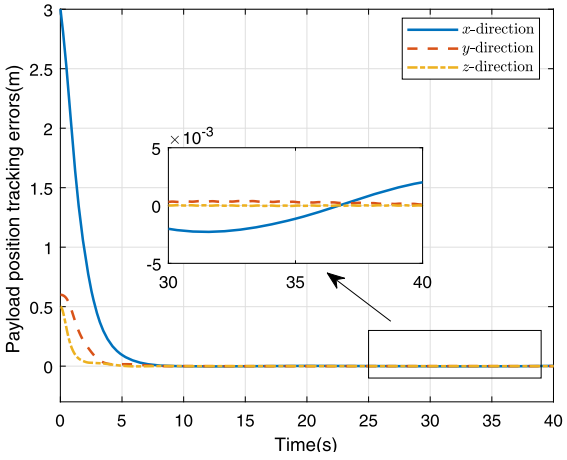

Fig. 10. Payload trajectory tracking errors under controller (37).

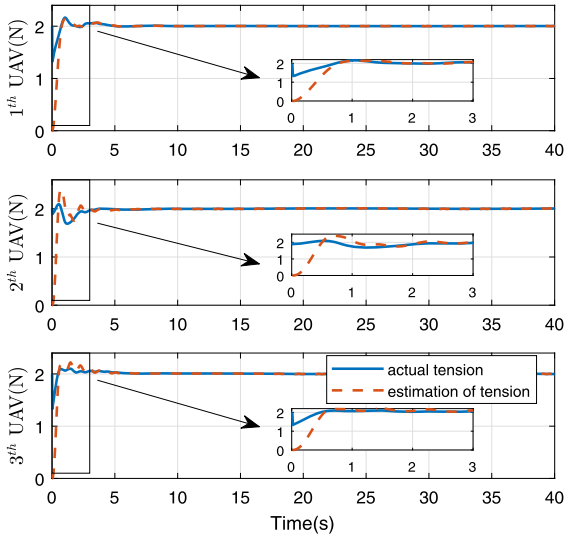

Fig. 11. Actual tension and its estimation on each tether.

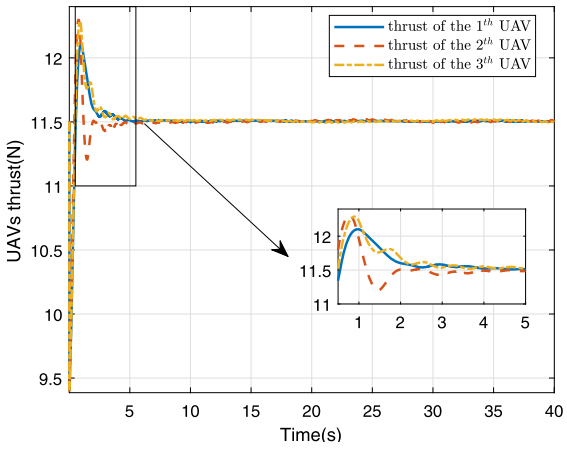

Fig. 12. Thrust of each UAVs.

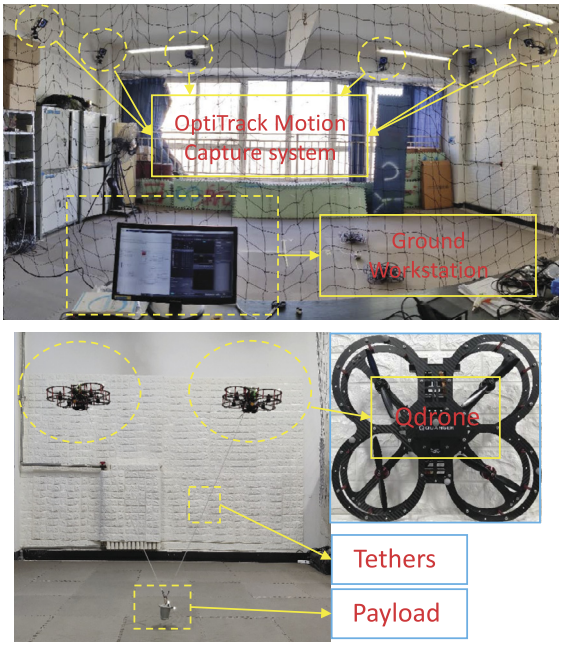

Fig. 13. The indoor experiment testbed.

Table 1
Physical parameters.

Parameters	Value	Parameters	Value
mass of QDrone (kg)	1.121	I_{xx} (kg m^2)	0.01
I_{yy} (kg m^2)	0.0082	I_{zz} (kg m^2)	0.0148
l_ϕ (m)	0.1068	l_θ (m)	0.0879
length of tether (m)	1.05	mass of payload (kg)	0.3

6. Experimental validation

6.1. Indoor experiment

The experimental facility consists of QDrone quadrotors, the OptiTrack motion capture system and a ground workstation. The indoor experiment testbed is shown in Fig. 13. In experiments, the desired trajectories of UAV1 and UAV2 are given as $r_{1d} = [0.5cos0.1t - 0.2; 0.5sin0.1t; 1.2]$ m, $r_{2d} = [0.5cos0.1t - 0.2 + 0.6\sqrt{3}; 0.5sin0.1t - 0.6; 1.2]$ m, respectively. The detailed physical parameters are shown in Table 1. To demonstrate the tracking stability, the system has flown for two trajectory cycles in this experiment. Moreover, some indexes are introduced to quantify the tracking accuracy. The mean absolute error $\bar{d}$ and the standard deviation σ are respectively defined as:

$$\bar{d} = \frac{1}{n}\sum_{i=1}^{n} \|r_i - r_{id}\| \tag{48}$$

$$\sigma = \sqrt{\frac{1}{n-1}\sum_{i=1}^{n}\left(\|r_i - r_{id}\| - \bar{d}\right)^2} \tag{49}$$

where r_i is the actual value, r_{id} is the desired value. The flight trajectories of UAVs with proposed algorithm and traditional PID are shown in Figs. 14 and 15. We can intuitively conclude that the tracking performance is better under our designed controller. The detailed results in Table 2 indicate that the steady-state performance of the proposed method is superior to that of the traditional PID controller, since the steady-state errors are generally less than that of the PID method. The standard deviations under proposed algorithm are apparently smaller than that of PID, which benefits from the fixed-time extended state observer for compensating the adverse effect of external disturbances caused by payload and wind generated by drones. The same conclusion can be derived from the max error in Table 2. Moreover, the controller designed by us only requires the position information. Both the position and velocity information are needed in PID controller. Therefore, the controller designed by us is better than PID controller. The video of experimental records under proposed method is uploaded in https://www.bilibili.com/video/BV14T4y1N7SP. The video of experiment under PID control is uploaded in https://www.bilibili.com/video/BV1L54y147Hy.

6.2. Outdoor experiment

In this section, an outdoor experiment with two quadrotors carrying a suspended payload is conducted to validate the proposed trajectory generation and motion control method. The experiment system consists of DJI-M210-RTK, LinkTrack UWB and a workstation. For the DJI-M210-RTK quadrotor, the NVIDIA Jetson TX2 compute board is used as the onboard computer. The angular velocity and attitude are obtained from inertial measurement unit. Positions of the quadrotors are measured from GPS and RTK at 10 Hz. The LinkTrack UWB system with four anchors on the ground and one tag in the payload (the payload is a box in this experiment) is used to measure the position of the payload. It should be noted that the proposed controller does not need the feedback of the payload state. The position information of payload is collected only for validation purpose. The LinkTrack UWB system can provide the position information at 50 Hz. Ground workstation sends the takeoff and landing command to quadrotors via the remote controller and receives the measurement date from LinkTrack UWB system. The real-time control is realized by the compute board on quadrotor with a sampling frequency of 10 Hz.

For safety, the desired relative distance between two quadrotors is set to be 15 m. An image of the two quadrotors successfully transporting a suspended payload is shown in Fig. 16. It should be noted that as the tether is attached to the quadrotor's tripod during the experiment, a moment would be resulted on the quadrotor body. Therefore, a conservative weight of payload is chosen to ensure that the quadrotor motors are not saturated with the extra moment. A light payload of approximately 1 kg is used in this experiment. The desired trajectory of payload is $r_{pd} = [10\sin(0.07\pi t); 8\cos(0.035\pi t); 4]$ m. The desired trajectory of quadrotor is generated in (24).

The experiment starts with the simultaneous takeoff of the two quadrotors controlled by the remote controller. After reaching the

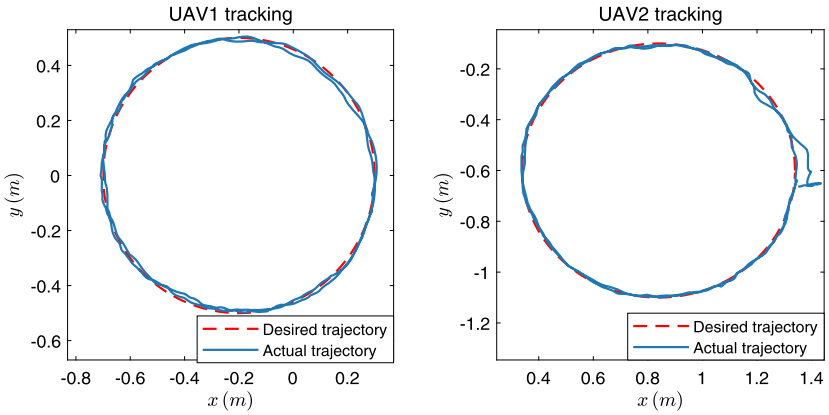

Fig. 14. Flight trajectories of UAVs in x and y directions with proposed algorithm.

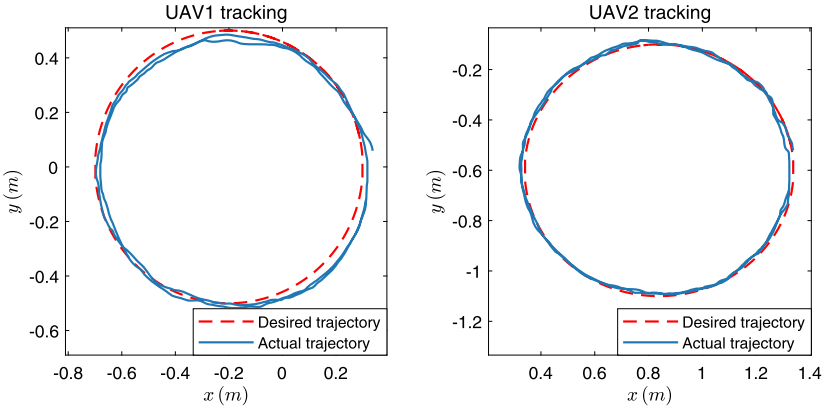

Fig. 15. Flight trajectories of UAVs in x and y directions with traditional PID.

Table 2
Steady-state performance of experiment (m).

UAV	Method	Mean error	Stand error	Max error
1	Proposed	0.0461 (↓)	0.0085 (↓)	0.0685 (↓)
1	PID	0.0488	0.0226	0.0808
2	Proposed	0.0426 (↓)	0.0062 (↓)	0.0617 (↓)
2	PID	0.0431	0.0122	0.0631

desired initial tracking positions, the quadrotors enter into the autonomous flight mode. In Figs. 17-20, the outdoor experiment results are shown. According to Figs. 17-18, both quadrotors and payload can track the desired figure-eight trajectory. At the same time, as can be seen on Fig. 19, the tracking errors of quadrotors remain relatively small during the entire experiment. The maximum tracking error existing along x-direction is approximately 1 m. The trajectory tracking error of payload is shown in Fig. 20. The maximum tracking error along x-direction is approximately 3 m, while it is about 1 m along y and z-direction. The completed video is uploaded in https://www.bilibili.com/video/BV1uv41147HT. The factors that affect the tracking accuracy are generalized as follows:

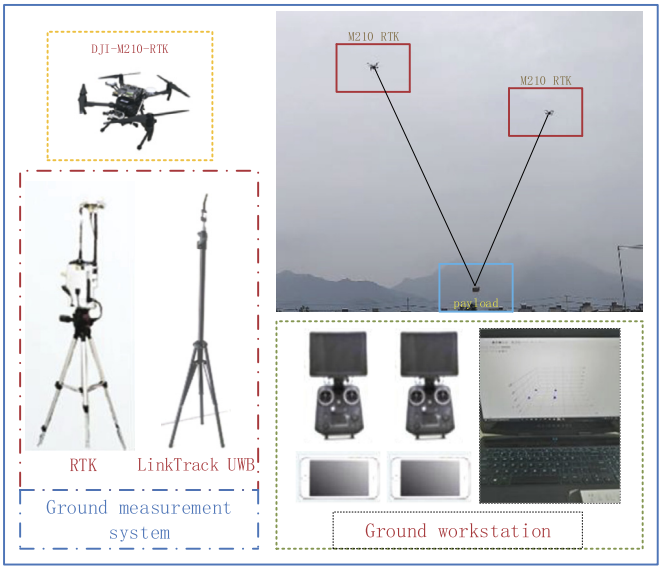

Fig. 16. Overview of the experimental system image of the experiment.

(1) In this experiment, only two quadrotors are used to carry a suspended payload. Accordingly, there is a swing along the motion direction. The tracking error of payload along the motion direction will be enlarged with the long tether.
(2) The tethered multi-rotor UAVs system is an under-actuated and strong coupling nonlinear system. Due to the winds in the outdoor environment, the swing of the tether system will be stimulated. The tracking error of payload will be enlarged without the feedback of payload states.
(3) The inaccurate parameters of payload mass, quadrotor mass, tether length, attachment point of tether on quadrotor will reduce the tracking accuracy.

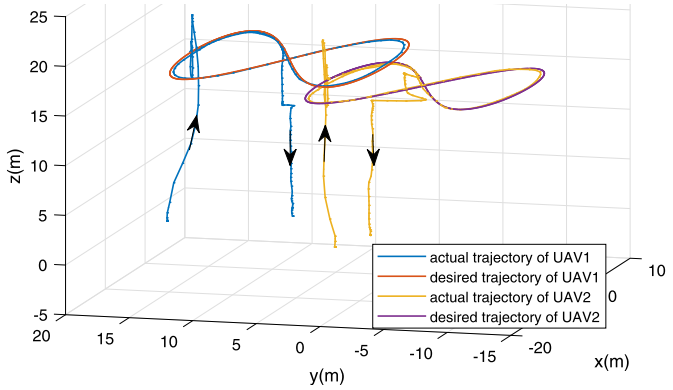

Fig. 17. Trajectories of UAVs in experiment.

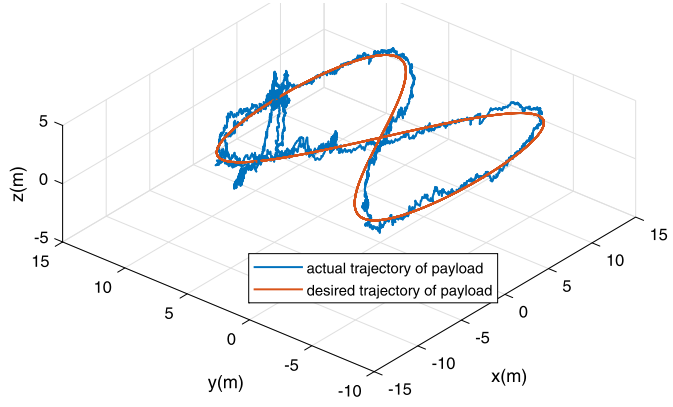

Fig. 18. Trajectory of payload in experiment.

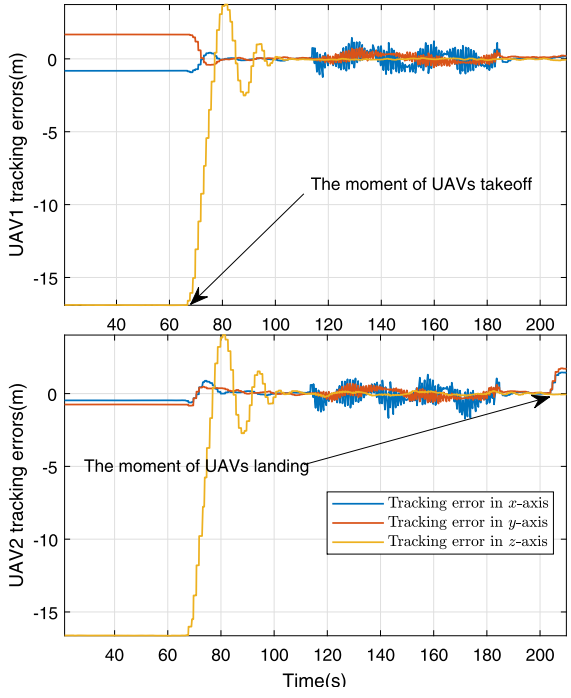

Fig. 19. Tracking errors of UAVs in experiment.

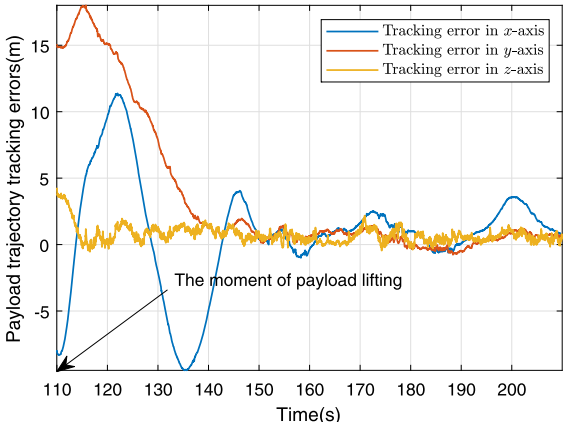

Fig. 20. Tracking errors of payload in experiment.

(4) In practice, the payload is not a strictly point mass. The rotation of payload will also influence the tracking result.

7. Conclusion

The dynamic available wrench set of the tethered multi-rotor UAVs system is analyzed and the corresponding capacity margin is introduced to evaluate the available maximum acceleration of the payload. These two indices can be used as a guidance for payload trajectory planning and system configuration design. Moreover, the feasible desired trajectories of UAVs are generated based on payload trajectory and the required tether tensions are derived with respect to the constraints of available wrench set, payload dynamics and collision avoidance between UAVs. The tension forces are calculated with the Udwadia-Kalaba equation and the completed system dynamics is constructed for simulation purpose. An output feedback controller based on fixed-time ESO is designed where only the position information of UAVs is needed. Finally, numerical simulations, indoor and outdoor flight experiments are conducted to validate the effectiveness of trajectory planning method and control strategy. All computations associated with the cooperative manipulation problem are implemented on UAVs' onboard computers in the outdoor experiment. A typical figure-eight curve is tested both in simulation and outdoor experiment. The simulation results show that the payload can track the desired figure-eight trajectory through controlling the UAVs to fly along the planned trajectory under the designed controller. The outdoor experiment also certificates the utility of designed planning and control methods. In the future, the trajectory planning for the payload within the available wrench space will be conducted. Moreover, the distributed trajectory optimization method proposed in [39] will be used to optimize the desired trajectories of UAVs online.

Declaration of competing interest

The authors declare that they have no known competing financial interests or personal relationships that could have appeared to influence the work reported in this paper.

Acknowledgements

This work was supported in part by the National Natural Science Foundation of China under Grant Nos. 91848205, 61725303, 61803313, in part by the Fundamental Research Funds for the Central Universities under Grant No. 3102019HTQD003 and in part by the Young Talent Fund of University Association for Science and Technology in Shaanxi, China under Grant No. 20190102.

Appendix A. Supplementary material

Supplementary material related to this article can be found online at https://doi.org/10.1016/j.ast.2021.106673.

References

[1] F. Liao, R. Teo, J. Wang, et al., Distributed formation and reconfiguration control of VTOL UAVs, IEEE Trans. Control Syst. Technol. 25 (1) (2017) 270–277.
[2] Y. Liu, P.F. Huang, F. Zhang, Y.K. Zhao, Distributed formation control using artificial potentials and neural network for constrained multiagent systems, IEEE Trans. Control Syst. Technol. 28 (2) (2020) 697–704.
[3] M. Kordestani, M. Dehghani, B. Moshiri, M. Saif, A new fusion estimation method for multi-rate multi-sensor systems with missing measurements, IEEE Access 8 (2020) 47522–47532.
[4] F. Ruggiero, V. Lippiello, A. Ollero, Aerial manipulation: a literature review, IEEE Robot. Autom. Lett. 3 (3) (2018) 1957–1964.
[5] A. Mohiuddin, T. Tarek, Y. Zweiri, D. Gan, A survey of single and multi-UAV aerial manipulation, Unmann Syst. 8 (2) (2020) 119–147.
[6] D.K. Villa, A.S. Brandao, M. Sarcinelli-Filho, A survey on load transportation using multirotor uavs, J. Intell. Robot. Syst. 98 (2020) 267–296.
[7] H. Lee, H. Kim, H.J. Kim, Planning and control for collision-free cooperative aerial transportation, IEEE Trans. Autom. Sci. Eng. 15 (1) (2018) 189–201.
[8] X. Liang, Y. Fang, N. Sun, H. Lin, Nonlinear hierarchical control for unmanned quadrotor transportation systems, IEEE Trans. Ind. Electron. 65 (4) (2018) 3395–3405.
[9] X. Liang, P. Zhang, Y. Fang, et al., Nonlinear control for aerial transportation systems with double-pendulum swing effects, IEEE Trans. Ind. Electron. (2021), https://doi.org/10.1109/TIE.2020.2998759, in press.
[10] B. Xian, S. Wang, S. Yang, An online trajectory planning approach for a quadrotor UAV with a slung payload, IEEE Trans. Ind. Electron. 67 (8) (2020) 6669–6678.
[11] K. Sreenath, N. Michael, V. Kumar, Trajectory generation and control of a quadrotor with a cable-suspended load–a differentially-flat hybrid system, in: Proc. IEEE Int. Conf. Robot. Autom, 2013, pp. 4888–4895.
[12] T. Lee, K. Sreenath, V. Kumar, Geometric control of cooperating multiple quadrotor UAVs with a suspended payload, in: Proc. IEEE Conf. Decision Control, 2013, pp. 5510–5515.
[13] T. Lee, Geometric control of quadrotor uavs transporting a cable-suspended rigid body, IEEE Trans. Control Syst. Technol. 26 (1) (2017) 255–264.
[14] F.A. Goodarzi, T. Lee, Dynamics and control of quadrotor UAVs transporting a rigid body connected via flexible cables, in: Proc. Amer. Control Conf., 2015, pp. 4677–4682.
[15] K. Sreenath, V. Kumar, Dynamics, control and planning for cooperative manipulation of payloads suspended by cables from multiple quadrotor robots, in: Proc. Robot., Sci. Syst., 2013.
[16] C. Masone, H.H. Bulthoff, P. Stegagno, Cooperative transportation of a payload using quadrotors: a reconfigurable cable-driven parallel robot, in: Proc. IEEE/RSJ Int. Conf. Intell. Robots Syst., 2016, pp. 1623–1630.
[17] L. Qian, H.H. Liu, Path following control of multiple quadrotors carrying a rigid-body slung payload, in: AIAA SciTech 2019 Forum, 2019, AIAA Paper 2019-1172.
[18] J. Fink, N. Michael, S. Kim, V. Kumar, Planning and control for cooperative manipulation and transportation with aerial robots, Int. J. Robot. Res. 30 (3) (2011) 324–334.
[19] N. Michael, J. Fink, V. Kumar, Cooperative manipulation and transportation with aerial robots, in: Proc. Robot.: Sci. Syst., Seattle, WA, 2009, pp. 73–86.
[20] K. Klausen, C. Meissen, T.I. Fossen, M. Arcak, T.A. Johansen, Cooperative control for multirotors transporting an unknown suspended load under environmental disturbances, IEEE Trans. Control Syst. Technol. 28 (2) (2020) 653–660.
[21] J. Geng, J.W. Langelaan, Cooperative transport of a slung load using load-leading control, J. Guid. Control Dyn. 43 (7) (2020) 1313–1331.
[22] X. Zhang, F. Zhang, P. Huang, et al., Distributed control for cooperative transportation in presence of unknown disturbance, in: Proc. IEEE Int. Conf. Real-Time Computing and Robotics, Irkutsk, Russia, 2019, pp. 772–777.
[23] J. Erskine, A. Chriette, S. Caro, Wrench analysis of cable-suspended parallel robots actuated by quadrotor unmanned aerial vehicles, J. Mech. Robot. 11 (2) (2019) 1–12.
[24] P. Bosscher, A. Riechel, I. Ebert-Uphoff, Wrench-feasible workspace generation for cable-driven robots, IEEE Trans. Robot. 22 (5) (2006) 890–902.
[25] M. Gouttefarde, D. Daney, J.P. Merlet, Interval analysis based determination of the wrench-feasible workspace of parallel cable-driven robots, IEEE Trans. Robot. 27 (1) (2011) 1–13.
[26] A. Rucco, P.B. Sujit, A.P. Aguiar, J.B. Sousa, F.L. Pereira, Optimal rendezvous trajectory for unmannned aerial-ground vehicles, IEEE Trans. Aerosp. Electron. Syst. 54 (2) (2018) 834–847.
[27] Y.G. Fu, M.Y. Ding, C.P. Zhou, H.P. Hu, Route planning for unmanned aerial vehicle (UAV) on the sea using hybrid differential evolution and quantum-behaved particle swarm optimization, IEEE Trans. Syst. Man Cybern. Syst. 43 (6) (2013) 1451–1465.
[28] B. Shirani, M. Najafi, I. Izadi, Cooperative load transportation using multiple UAVs, Aerosp. Sci. Technol. 84 (2019) 158–169.
[29] W. Gong, B. Li, Y. Yang, H. Ban, B. Xiao, Fixed-time integral-type sliding mode control for the quadrotor UAV attitude stabilization under actuator failures, Aerosp. Sci. Technol. 95 (2019) 105444.
[30] T. Menard, E. Moulay, W. Perruquetti, Fixed-time observer with simple gains for uncertain systems, Automatica 81 (2017) 438–446.
[31] F. Lopez-Ramirez, A. Polyakov, D. Efimov, W. Perruquetti, Finitetime and fixed-time observer design: implicit Lyapunov function approach, Automatica 87 (2018) 52–60.
[32] Y. Liu, F. Zhang, P. Huang, Y. Lu, Fixed-time consensus tracking for second-order multiagent systems under disturbance, IEEE Trans. Syst. Man Cybern. Syst. (2021), https://doi.org/10.1109/TSMC.2019.2944392, in press.
[33] A. Levant, High-order sliding modes: differentiation and output feedback control, Int. J. Control 76 (9) (2003) 924–941.
[34] M.T. Angulo, J.A. Moreno, L. Fridman, Robust exact uniformly convergent arbitrary order differentiator, Automatica 49 (2013) 2489–2495.
[35] F. Kendoul, Nonlinear hierarchical flight controller for unmanned rotorcraft: design, stability, and experiments, J. Guid. Control Dyn. 32 (6) (2009) 1954–1958.
[36] Z.H. Cai, H. Zhou, J. Zhao, K. Wu, Y.X. Wang, Formation control of multiple unmanned aerial vehicles by event-triggered distributed model predictive control, IEEE Access 6 (2018) 55614–55627.
[37] Y. Xu, Z.G. Wu, Distributed adaptive event-triggered fault-tolerant synchronization for multi-agent systems, IEEE Trans. Ind. Electron. 68 (2) (2020) 1537–1547.
[38] Y. Xu, M. Fang, Y.J. Pan, et al., Event-triggered output synchronization for non-homogeneous agent systems with periodic denial-of-service attacks, Int. J. Robust Nonlinear Control (2021), https://doi.org/10.1002/rnc.5223, in press.
[39] Y. Kuwata, J.P. How, Cooperative distributed robust trajectory optimization using receding horizon MILP, IEEE Trans. Control Syst. Technol. 19 (2) (2011) 423–431.